

# Neuromorphic LiDAR-based Bird’s Eye View Object Detection using Energy-efficient Spiking Neural Networks

Sambit Mohapatra<sup>1,3</sup>, Senthil Yogamani<sup>2</sup>, Heinrich Gotzig<sup>1</sup> and Patrick Mäder<sup>3</sup>  
<sup>1</sup>Valeo, Germany <sup>2</sup>Valeo, Ireland <sup>3</sup>TU Ilmenau, Germany

**Abstract**—Autonomous driving perception demands accurate and efficient processing of three-dimensional sensor data under strict power constraints. Traditional convolutional neural networks achieve strong detection accuracy but are computationally intensive, limiting their suitability for deployment on resource-constrained neuromorphic platforms. Spiking neural networks offer a compelling alternative through event-driven sparse computation, yet their application to complex real-world perception tasks such as three-dimensional object detection remains limited. In this work, we propose an end-to-end spiking encoder-decoder network for object detection in bird’s eye view representations of LiDAR point clouds, trained using surrogate gradient backpropagation. We train two variants: a membrane potential variant that reads continuous neuron state at the output stage for maximum accuracy, achieving 92.05/87.04/86.51 AP at IoU = 0.5 (Easy/Moderate/Hard), and, a fully binary spiking variant that operates exclusively on spike trains at every layer for direct neuromorphic deployment. We evaluate four input spike encoding strategies and demonstrate that allowing the network to learn spike representations directly from data outperforms hand-crafted Poisson, latency, and z-axis encoding schemes on the KITTI benchmark, where sequential frames are unavailable and the BEV input is presented repeatedly across timesteps as a proxy for temporal streaming. A block-wise energy analysis demonstrates a 3.33× reduction in synaptic operation energy over an equivalent CNN under conservative loop-based operation. Together, these results demonstrate the viability of spiking neural networks for accurate and energy-efficient neuromorphic perception in autonomous driving.

## I. INTRODUCTION

Object detection is a fundamental task in autonomous driving and advanced driver assistance systems, with direct impact on downstream functions including collision avoidance, path planning, and driving decision making [1]. LiDAR sensors have become central to state-of-the-art three-dimensional object detection pipelines, providing dense and accurate spatial measurements of the environment that enable robust perception under varying lighting and atmospheric conditions compared to depth from cameras [2].

Convolutional neural networks (CNNs) have been the dominant paradigm for processing LiDAR point clouds. Three-dimensional CNN architectures operate directly on voxelized point clouds using 3D convolutions, while 2D approaches project the point cloud into compact representations such as bird’s eye view (BEV) images or range images, enabling faster inference through 2D convolutions. Despite their accuracy, CNNs process every spatial location in the sensor field of view with equal computational weight. For sparse inputs such as LiDAR BEV maps—where the majority of cells contain no returns—this leads to significant wasted computation and

energy, processing empty cells with the same cost as informative measurements. Furthermore, the inherently frame-based operating principle of CNNs does not differentiate between information-rich regions and redundant background, nor does it exploit temporal persistence across consecutive sensor frames.

Spiking neural networks (SNNs) offer a principled solution to these limitations by drawing inspiration from biological neural computation. Information is represented and communicated as discrete binary spikes, replacing the multiply-accumulate (MAC) operations of CNNs with conditional accumulate-only (AC) operations that are triggered exclusively by spike events. Since inactive neurons contribute no synaptic operations, the computational cost scales directly with the firing sparsity of the network rather than its total capacity—a property that is particularly advantageous for sparse inputs such as LiDAR BEV maps. Beyond computational sparsity, spiking neurons maintain internal state through their membrane potential, which integrates incoming spikes across multiple timesteps. This temporal integration allows the network to accumulate evidence progressively, suppressing transient noise and reinforcing persistent spatial features. On neuromorphic hardware platforms such as Intel Loihi 2 [3], IBM TrueNorth [4], and SpiNNaker [5], these properties translate directly into measurable energy savings. The replacement of MAC with AC operations alone reduces per-synaptic-event energy by a factor of approximately 5× at 45 nm process technology [6], and this saving compounds multiplicatively with network sparsity.

These properties become increasingly relevant as automotive sensor technology advances toward higher frame rates and event-driven modalities. Next-generation solid-state LiDAR sensors are targeting scan rates well beyond the 10–20 Hz of current rotating systems [7], and event cameras operating at megahertz temporal resolution are beginning to appear in automotive perception research [8]. Radars are sparser than LiDARs and CNNs are less efficient [9]. For CNN-based pipelines, higher frame rates translate directly to proportionally higher computational and energy costs, since every frame requires a complete forward pass at full precision regardless of how much the scene has changed between frames. SNNs are architecturally well-suited to this trend: the timesteps map naturally onto the sensor frame rate, each new measurement advancing the membrane potential integration by one step rather than triggering a complete recomputation from scratch. This temporal and energetic scalability positions SNNs as a particularly promising architecture for the high-rate, event-driven sensing pipelines that next-generation autonomous vehi-

cles will rely upon. While the experiments in this work operate on pre-recorded static frames from an established benchmark, the architecture is designed with sequential deployment in mind: the temporal window maps directly onto a live sensor stream in a deployed system, where each incoming frame naturally advances the spiking dynamics without any explicit frame repetition.

Despite these theoretical advantages, SNNs remain predominantly applied to classification tasks, with only a small number of published works addressing complex real-world perception tasks such as 3D object detection, which requires multi-scale feature extraction, simultaneous regression and classification outputs, and operation on large high-resolution spatial maps. This gap is significant: the perception tasks that would benefit most from the energy efficiency of SNNs are precisely those that have proven most challenging to port from CNN architectures.

This paper addresses this gap directly. We propose an end-to-end spiking encoder-decoder network for object detection in BEV of LiDAR point clouds from the KITTI benchmark [10], trained using surrogate gradient backpropagation implemented in the `snn_torch` library [11]. We demonstrate that spiking neural networks can match the detection accuracy of full-precision CNNs while consuming a fraction of their inference energy, and that the accuracy–efficiency trade-off historically associated with SNN-based perception can be substantially reduced through careful architecture design, spike-domain loss functions, and training configuration.

The main contributions of this work are as follows:

- We propose a spiking encoder-decoder architecture for bird’s eye view LiDAR object detection that integrates spatial feature extraction with the temporal dynamics of leaky integrate-and-fire neurons, enabling low-power event-driven processing of sparse BEV maps.
- We present solutions to the key challenges of applying SNNs to complex perception tasks, including end-to-end surrogate gradient training and two novel spike-domain loss functions: (i) a *two-point temporal BCE and Dice loss* for keypoint detection that supervises both early and full temporal windows of spike activity to enforce spatial coherence of object-center predictions, and (ii) a *population-coded spike regression loss* for bounding box estimation that encodes continuous physical dimensions through the collective firing rate of a local  $k \times k$  neuron population—eliminating the need to discretise regression targets into bins. Rotation prediction is formulated as a spike-compatible classification task over discretised orientation bins.
- We train and evaluate two inference variants—membrane potential and fully binary spiking—demonstrating that the fully spiking variant achieves competitive detection accuracy with no continuous-valued activations at any stage.
- We conduct a comprehensive block-wise synaptic energy analysis by mapping layer-wise firing rates to a 45 nm technology energy model, quantifying a  $3.33\times$  inference energy reduction over an equivalent CNN under conservative loop-based simulation—rising to an estimated  $43\times$

on dedicated neuromorphic hardware—and identifying the accumulate-only operation substitution and 88.19% firing sparsity as the two independent mechanisms driving this gain.

## II. RELATED WORK

### A. LiDAR-Based 3D Object Detection

LiDAR-based 3D object detection has been dominated by CNN architectures operating on voxelized or projected representations of point clouds. Early volumetric methods such as Vote3Deep [12] and VoxelNet [13] apply sparse 3D convolutions on voxelized point clouds, while SECOND [14] accelerates this pipeline through improved sparse convolution algorithms. Although accurate, 3D convolutional architectures are computationally expensive and scale poorly with field-of-view, driving interest in more efficient 2D projection-based approaches.

Two-stage methods such as PointRCNN [15] generate region proposals from the raw point cloud using PointNet++ [16] and refine them in a second stage, achieving strong accuracy at the cost of latency. PV-RCNN [17] further improves precision by fusing point-level and voxel-level features into keypoint representations, but the two-stage design remains a bottleneck for real-time deployment.

Bird’s eye view (BEV) representations offer a practical alternative: they preserve metric scale and aspect ratios, naturally accommodate dense point clouds without increasing map resolution, and enable efficient 2D convolutions. PointPillars [18] encodes point clouds into vertical pillars using PointNet [19], learning dense features over sparse BEV grids and remains a strong real-time baseline. PIXOR [20] introduced an anchor-free BEV detector using a BEV occupancy map, demonstrating that simple 2D convolutional backbones can achieve real-time 3D detection without anchor regression overhead. BEVDetNet [21] extends this with anchor-free keypoint-based object center detection, achieving low inference latency with competitive accuracy on KITTI [10]. More recently, Naich et al. [22] proposed enhanced voxel feature construction via intensity histograms, though the 3D backbone limits real-time suitability. Lis et al. [23] introduced a fully quantized INT8 pipeline targeting FPGA deployment, demonstrating that hardware-aware design constraints can yield significant efficiency gains without sacrificing accuracy.

Despite these advances, all of these methods operate on dense floating-point activations and perform a full forward pass for every input frame regardless of scene content. This frame-based, activation-dense processing is fundamentally mismatched to the inherent sparsity of LiDAR data, where the majority of the BEV map contains no returns. These inefficiencies motivate the application of spiking neural networks, which compute only where spike events occur.

### B. Spiking Neural Networks for Perception

1) **ANN-to-SNN Conversion:** Early SNN perception methods circumvented the difficulty of direct training by converting pre-trained CNNs to SNNs. Cao et al. [24] and Diehl et al. [25] demonstrated that CNNs trained on simple datasets could be

converted to functional SNNs, but required large numbers of timesteps to approximate the continuous activations of the source network, making real-time deployment impractical. Rueckauer et al. [26] broadened the conversion repertoire by proposing spiking equivalents of pooling, batch normalization, and other standard CNN blocks, enabling conversion of complex architectures trained on ImageNet [27] and CIFAR-10 [28]. Kim et al. [29] applied conversion to image-based object detection on a challenging dataset [30], introducing signed neurons and channel-wise normalization to handle the signed activations that detection requires. More recently, Qu et al. [31] substantially reduced the timestep requirement of conversion-based detectors through time-varying spike thresholds, narrowing the accuracy gap at practical latencies.

For 3D point cloud perception, SpikiLi [32], our prior work, applied conversion to BEV-based LiDAR object detection, demonstrating the feasibility of SNN inference on point clouds. However, as with other conversion methods, accuracy is bounded by the pre-trained CNN weights and the approximation errors introduced during conversion. Tao et al. [33] extended conversion to point cloud classification using spike-based X-convolutions [34]. Lan et al. [35] improved conversion fidelity through KL-divergence-based threshold initialization to align spike activations with ReLU outputs, achieving nearly lossless conversion for classification tasks. A fundamental limitation of all conversion-based approaches is that they inherit the architectural constraints of the source CNN and cannot exploit the temporal integration properties of spiking neurons during training, limiting both accuracy and energy efficiency.

2) **Directly Trained SNNs**: Direct training of SNNs using surrogate gradients [36] and spatio-temporal backpropagation [37] has produced significantly stronger results than conversion, since the network is optimized end-to-end for spike-based computation. This allows the network to learn representations that are inherently sparse and temporally structured rather than approximating a pre-trained dense network.

For 2D object detection, Li et al. [38] proposed multi-scale spiking feature fusion achieving a strong energy-efficient benchmark, while Cordone et al. [39] demonstrated directly trained SNNs reaching competitive detection performance on vehicular image datasets with up to 85% energy savings over equivalent CNNs. Zhu et al. [40] presented Spiking Autonomous Driving (SAD), the first unified end-to-end SNN addressing perception, prediction, and planning for autonomous driving, underscoring the growing maturity of directly trained SNNs for complex driving tasks.

For 3D point cloud perception, Ren et al. [41] introduced Spiking PointNet, the first spiking model for deep learning directly on point clouds, trained with a single timestep but achieving improved performance with multiple timesteps at inference. Wu et al. [42] proposed point-to-spike residual learning for 3D point cloud classification, designing spatial-aware kernel point spiking neurons that relate spike generation to 3D point position and stacking them into residual blocks for energy-efficient feature learning.

For 3D detection, SpikeCloudNet [43] applies direct training to point cloud detection and reports competitive accuracy

on KITTI, representing the strongest directly-trained SNN baseline for this task. Lian et al. [44] proposed DeepSCNN, integrating a spiking convolutional network with temporal coding into the YOLOv2 architecture and developing a novel preprocessing layer to translate 3D point cloud data into spike time data, demonstrating SNN applicability to real-time LiDAR detection. However, none of these works address the challenge of performing continuous regression directly from binary spike outputs for 3D bounding box estimation—instead relying on membrane potential readout or discretization schemes that either require continuous-valued activations or sacrifice precision. Furthermore, energy efficiency claims in prior work are typically made at the network level without a block-wise synaptic operation analysis that traces the origin of savings to individual architectural stages.

Our work addresses these gaps by proposing a fully end-to-end spiking network for LiDAR BEV detection trained from scratch. We introduce novel spike-domain loss functions for keypoint detection and population-coded bounding box regression that operate directly on spike rates. Furthermore, we provide a comprehensive block-wise energy analysis that quantifies the efficiency contribution of each individual encoder and decoder stage. Furthermore, we provide a comprehensive block-wise energy analysis quantifying a  $3.33\times$  reduction in synaptic operation energy over an equivalent CNN under conservative simulation conditions, rising to an estimated  $43\times$  on dedicated neuromorphic hardware, with savings traced to individual encoder and decoder stages.

### III. BACKGROUND

Neuromorphic computing draws inspiration from the signal processing principles of biological neural systems to achieve ultra-low-power event-driven computation. Spiking neural networks (SNNs) form the algorithmic foundation of neuromorphic computing, communicating information via discrete binary spikes—analogue to the voltage pulses of biological neurons—rather than the continuous activations of conventional networks.

#### A. Spiking Neuron Models

Unlike conventional neural networks that process inputs in a single forward pass, spiking neural networks operate over discrete timesteps, with neurons integrating incoming spikes across time and emitting output spikes when their membrane potential exceeds a threshold. Synaptic weights play the role of biological synapses, scaling the contribution of each presynaptic spike to the postsynaptic neuron’s membrane potential. Several neuron models exist, trading off biological fidelity against computational tractability.

a) **Integrate-and-Fire Model**: The simplest spiking neuron model integrates incoming weighted inputs into a membrane potential  $V(t)$  and emits a spike when  $V(t)$  exceeds a threshold  $V_{\text{thr}}$ , after which the potential is reset. The model has no leak term, meaning the membrane retains all accumulated charge indefinitely in the absence of a spike. While computationally simple, this makes the neuron sensitive to input history over arbitrarily long windows, which can destabilise training on long sequences.

*b) Leaky Integrate-and-Fire Model:* The Leaky Integrate-and-Fire (LIF) model is the most widely adopted spiking neuron model for deep SNN training due to its balance between biological plausibility and computational tractability [45], and is the neuron model adopted throughout this work. Biologically, a neuron maintains a voltage difference across its cell membrane, known as the membrane potential  $V(t)$ , which fluctuates as it integrates electrical charges from incoming spikes. In continuous time, the membrane dynamics are governed by:

$$\tau_m \frac{dV(t)}{dt} = -(V(t) - V_{\text{rest}}) + RI(t), \quad (1)$$

where  $\tau_m = RC$  is the membrane time constant,  $R$  the membrane resistance,  $C$  the membrane capacitance,  $V_{\text{rest}}$  the resting potential, and  $I(t)$  the total synaptic input current. The leakage term  $-(V(t) - V_{\text{rest}})$  decays the membrane potential toward rest in the absence of input, conferring temporal memory that is absent in stateless CNN activations.

Setting  $V_{\text{rest}} = 0$  and discretizing for software simulation, the update equation implemented in `snntorch` [11] is:

$$U[t+1] = \beta U[t] + WX[t+1] - S[t]U_{\text{thr}}, \quad (2)$$

where  $U[t]$  is the membrane potential at timestep  $t$ ,  $\beta \in (0, 1)$  is the learnable decay factor controlling the rate of membrane leakage,  $WX[t+1]$  is the weighted presynaptic spike input, and  $-S[t]U_{\text{thr}}$  implements a subtract-and-continue reset: when a spike  $S[t] = 1$  is emitted (i.e.  $U[t] \geq U_{\text{thr}}$ ), the threshold voltage is subtracted from the membrane potential rather than resetting it to zero, allowing any suprathreshold charge to carry forward into the next timestep. A spike is generated according to the Heaviside step function:

$$S[t] = \Theta(U[t] - U_{\text{thr}}), \quad (3)$$

where  $U_{\text{thr}}$  is the learnable spike threshold. Both  $\beta$  and  $U_{\text{thr}}$  are optimized end-to-end during training in our implementation.

### B. Spike Coding

Spike coding defines how continuous-valued sensor data are converted into binary spike trains for SNN processing.

*a) Rate coding:* encodes information in the spike count over a time window. For a normalized input  $x \in [0, 1]$ , Poisson encoding [46] generates a spike at each timestep with probability:

$$P(S[t] = 1) = x. \quad (4)$$

While robust, rate coding requires large  $T$  to represent high-precision values accurately, increasing latency and energy cost [45].

*b) Temporal coding:* encodes information in spike timing rather than count. In time-to-first-spike (TTFS) encoding [47], larger inputs produce earlier spikes. This is highly energy-efficient but yields very sparse inputs that are difficult to train with gradient-based methods and are sensitive to noise.

*c) Direct coding:* avoids fixed probabilistic or temporal schemes by passing continuous inputs directly as injection current to the first spiking layer, allowing the network to learn an optimal task-specific encoding from data [48]. This approach preserves input precision and consistently outperforms hand-crafted coding schemes for complex tasks. In this work we adopt a self-coding variant of direct coding, in which the same BEV frame is presented identically at each of the  $T$  timesteps, allowing LIF neurons to integrate evidence across repeated presentations and converge to a stable internal representation. As confirmed by our ablation in Table IV, this outperforms Poisson, latency, and z-axis encoding schemes for BEV-based detection.

### C. Training with Surrogate Gradients

Training SNNs with gradient descent is complicated by the non-differentiability of the spike generation function (Eq. 3): the Heaviside step has zero derivative everywhere except at the threshold, blocking gradient flow through the network. The surrogate gradient method [36] resolves this by substituting a smooth differentiable function  $\hat{\sigma}'$  for the true derivative during the backward pass:

$$\frac{\partial S}{\partial U} \approx \hat{\sigma}'(U - U_{\text{thr}}). \quad (5)$$

We use a tanh-based surrogate gradient implemented in `snntorch` [11]:

$$\hat{\sigma}'(x) = 1 - \tanh^2(kx), \quad (6)$$

where  $k$  controls the sharpness of the approximation. Note that  $\hat{\sigma}'(x)$  is the derivative of  $\tanh(kx)/k$ , which closely approximates the Heaviside step near the threshold and decays smoothly away from it. Gradients are propagated through time via spatio-temporal backpropagation (STBP) [37], which unrolls the network across  $T$  timesteps and accumulates gradients over the full simulation window.

### D. Output Decoding

Output decoding defines the interface between binary spike trains and the real-valued predictions required by downstream tasks.

*a) Rate decoding:* uses the mean firing rate  $\bar{S} = \frac{1}{T} \sum_{t=1}^T S[t]$  as a continuous output proxy. The class with the highest firing rate is taken as the predicted category for classification tasks. Precision is limited to  $1/T$  for regression, making it unsuitable for direct continuous value estimation.

*b) Membrane potential decoding:* removes the spike threshold from the output layer, allowing the membrane potential to accumulate continuously without resetting. The resulting floating-point value is decoupled from  $T$  and is well-suited for regression. We adopt this for the vmem inference variant of our model.

c) **Discretized regression**: converts a continuous regression target into  $C$  uniform bins, where  $C$  is the number of classes, transforming the problem into a classification task [11]. The predicted class is obtained via:

$$\hat{k} = \arg \max_c \operatorname{softmax} \left( \frac{1}{T} \sum_{t=1}^T S_{\text{out},c}[t] \right), \quad (7)$$

which is effective even at small  $T$  since only a relative ordering of firing rates is required. We apply this for rotation prediction (31 bins of  $6^\circ$ ).

d) **Population-coded regression**: encodes a continuous value through the collective mean firing rate of a local  $k \times k$  neuron cluster rather than the output of a single neuron [49]. This allows direct spike-based regression without discretization and is the approach we adopt for bounding box dimension prediction, where the  $\log_{10}$ -transformed target dimensions  $[\log_{10}(H), \log_{10}(W), \log_{10}(L)]$  are decoded from the mean firing rate of a local neuron population at each keypoint location, as described in Section IV-C2.

#### IV. PROPOSED METHOD

BEV-based CNN detectors achieve computational efficiency through 2D convolutions on projected point cloud representations, avoiding the cost of 3D volumetric processing. We aim to augment this computational efficiency with inference energy efficiency by replacing dense activations with binary spike trains. A key departure from our prior CNN to SNN conversion work [32] is the adoption of direct training with surrogate gradients. Conversion-based methods inherit the accuracy ceiling of the source network and introduce approximation errors that limit SNN performance. By training end-to-end from scratch, the network is free to learn spike-based representations optimised for the detection task directly. Combined with careful network architecture design and novel spike-domain loss functions, we aim to bring SNN detection accuracy close to full-precision CNN baselines while maintaining substantial inference energy efficiency gains. The following subsections describe the input representation, network architecture, and loss functions that together realise these goals.

##### A. Input Preparation

Raw LiDAR point clouds are inherently sparse and unstructured, making direct neural network processing compute-intensive and poorly suited to real-time embedded deployment. Following [21], [50]–[52], we project the 3D point cloud into a 2D bird’s eye view (BEV) representation. A  $60 \text{ m} \times 60 \text{ m}$  ground-plane range is discretized at a cell resolution of  $\Delta = 0.1875 \text{ m}$ , yielding a spatial grid of  $320 \times 320$  cells. For each 3D point  $\mathbf{p} = (x, y, z, i)$ , the grid indices are:

$$r = \left\lfloor \frac{x_{\max} - x}{\Delta} \right\rfloor, \quad c = \left\lfloor \frac{y_{\max} - y}{\Delta} \right\rfloor, \quad (8)$$

where  $(x_{\max}, y_{\max})$  are the upper bounds of the covered range. All  $z$  values are shifted by  $|z_{\min}|$  to start from zero before feature computation.

Five geometric and reflectance features are computed per pillar from all points mapped to it: maximum height ( $z_{\max}$ ),

binary occupancy ( $d$ ), mean reflectance intensity ( $\bar{i}$ ), minimum height ( $z_{\min}$ ), and height standard deviation ( $\sigma_z$ ), computed via the Welford online algorithm for numerical stability. These form the primary BEV map  $\mathbf{I}_{\text{BEV}} \in \mathbb{R}^{320 \times 320 \times 5}$ . All five channels are normalized to  $[0, 1]$  using fixed physical bounds: heights by the shifted  $z$  range, binary occupancy is already in  $\{0, 1\}$ , intensity is clipped to  $[0, 1]$  directly from the Velodyne sensor range, and  $\sigma_z$  is normalized by half the shifted  $z$  range, since the standard deviation of a bounded variable cannot exceed half its range. Empty pillars are explicitly zeroed after normalization.

To preserve vertical structure within each pillar, the  $z$ -axis is uniformly discretized into  $K = 6$  height bins spanning ground level to 2.4 m, covering the full height range of passenger vehicles. An auxiliary binary occupancy map  $\mathbf{Z}_{\text{BEV}} \in \{0, 1\}^{320 \times 320 \times 6}$  records the presence of at least one point in each bin at every pillar. The two representations are concatenated along the channel dimension to form the full network input:

$$\mathbf{X} = [\mathbf{I}_{\text{BEV}} \parallel \mathbf{Z}_{\text{BEV}}] \in \mathbb{R}^{320 \times 320 \times 11}, \quad (9)$$

giving  $C = 11$  input channels, consistent with the network input shape reported in Table V.

##### B. Network Architecture

1) **Overview**: The proposed network is an encoder-decoder architecture following the U-Net [53] design principle, adapted for spiking computation. The input tensor  $\mathbf{X} \in \mathbb{R}^{320 \times 320 \times 11}$  is first processed by a stem convolutional layer followed by a LIF neuron layer, converting the continuous BEV map into a spike representation via the self-coding strategy described in Section III-B. All intermediate activations throughout the network are binary spike trains  $\mathbf{S} \in \{0, 1\}^{T \times B \times C \times H \times W}$  (where  $B$  is the batch size,  $C$  the channel count, and  $H \times W$  the spatial resolution), processed over  $T = 13$  timesteps. The value of  $T = 13$  was determined empirically. Increasing  $T$  beyond 13 exceeded GPU memory capacity at a batch size of 4 at  $320 \times 320$  resolution. Additionally, longer unrolled sequences increase the risk of vanishing gradients during spatio-temporal backpropagation, as surrogate gradients attenuate with each additional timestep. Training time also scales linearly with  $T$ , making larger values impractical within the available compute budget.  $T = 13$  represents the largest value satisfying all three constraints simultaneously.

2) **Encoder**: The encoder comprises four downsampling blocks (DB1–DB4) that progressively extract features at decreasing spatial resolutions. Each DB contains two Conv|GN|LIF stages followed by a channel-concatenation skip connection and a strided pooling convolution. The first convolution uses a  $5 \times 5$  kernel to capture the spatial extent of objects at each scale. The output of the second Conv|GN|LIF stage is concatenated with the block input along the channel dimension ( $\otimes$ ), preserving the original feature map before pooling. A final strided convolution halves the spatial resolution to  $H/2 \times W/2$ . Each DB therefore produces two outputs: a full-resolution skip feature map passed to the corresponding decoder block, and a half-resolution feature map passed to

the next encoder stage. Group normalisation (GN) is used throughout in place of batch normalisation (BN), as it is independent of batch size and behaves identically at training and inference time—an important property for neuromorphic deployment where batch size is typically one.

3) **Decoder**: The decoder comprises four upsampling blocks (UB) arranged in a bottom-up path from the bottleneck to full resolution. Each UB receives the skip feature map from its corresponding encoder level and the upsampled feature map from the previous decoder stage, concatenates them ( $\otimes$ ), and processes the joint representation through a Conv|GN|LIF stage. Spatial upsampling is performed by a transposed convolution followed by GN, doubling the spatial resolution at each stage. This hierarchical aggregation allows the decoder to combine fine-grained spatial information from early encoder stages with semantically rich features from the bottleneck, which is particularly important for accurate keypoint localisation on the sparse BEV map.

4) **Output Heads**: Three parallel spiking output heads operate on the full-resolution decoder output. Each head consists of a single Conv|LIF stage with no intermediate normalisation, allowing the membrane potential to accumulate freely across timesteps without normalisation interference.

a) **Keypoint head**: Predicts object-centre heatmaps from which keypoint locations are decoded. Objects are represented as Gaussian heatmap targets with unit peak at their projected ground-plane centres, decaying spatially to suppress background firing in the vicinity of object locations. The head is supervised by the two-point temporal focal and masked Dice loss described in Section IV-C1.

b) **Box head**: Predicts bounding box dimensions  $[\log_{10}(h), \log_{10}(w), \log_{10}(l)]$  at keypoint locations. The  $\log_{10}$  transformation maps typical car dimensions (0.5–10 m) to  $[0, 1]$ , making the regression target compatible with spike-rate outputs. Dimensions are supervised by the population-coded spike regression loss described in Section IV-C2.

c) **Rotation head**: Predicts heading orientation as a classification over 31 uniform bins of  $6^\circ$  each, covering  $[0, \pi]$  to exploit the rotational symmetry of the BEV representation. A bin width of  $6^\circ$  provides sufficient angular resolution for vehicle orientation estimation in BEV while remaining reliably learnable within  $T=13$  timesteps. Label smoothing of  $\varsigma=0.1$  is applied to reflect the geometric similarity of adjacent orientation bins. The head is supervised by the masked cross-entropy loss described in Section IV-C3.

### C. Losses

1) **Keypoint Detection Loss**: The keypoint detection head produces spike trains  $\mathbf{S}_{\text{kp}} \in \{0, 1\}^{T \times B \times 1 \times H \times W}$ . Object centres are represented as Gaussian heatmap targets  $\mathbf{Y}_{\text{kp}}^* \in [0, 1]^{B \times H \times W}$ , with unit peak at each object centre decaying spatially with a Gaussian kernel. Keypoint peaks typically constitute less than 1% of the spatial map, creating severe class imbalance between object-centre and background pixels. The proposed loss  $\mathcal{L}_{\text{kp}}$  addresses this through two components, both operating on temporally aggregated spike rates. Table I defines the notation used throughout this section.

TABLE I: Notation Summary for  $\mathcal{L}_{\text{kp}}$

Symbol	Description
$T$	Number of timesteps
$\alpha_t$	Early window fraction
$T_e$	Early window steps $\lfloor \alpha_t T \rfloor$
$k$	ROI dilation radius
$\mathbf{S}_{\text{kp}}^{(t)}$	Binary spike tensor at timestep $t$
$\hat{\mathbf{R}}_e$	Early-window mean firing rate map
$\hat{\mathbf{R}}_f$	Full-window mean firing rate map
$\mathbf{Y}_{\text{kp}}^*$	Ground-truth Gaussian heatmap
$\alpha, \beta$	Focal loss exponents
$w_e, w_f$	Early and full window focal weights
$\mathbf{M}_{\text{roi}}$	Dilated keypoint ROI mask
$\tilde{\mathbf{r}}_b, \tilde{\mathbf{y}}_{\text{kp}, b}^*$	Masked rate and GT for item $b$
$\epsilon$	Dice smoothing constant
$\lambda_d$	Masked Dice loss weight
$e, e_{\text{gate}}$	Current epoch; Dice activation epoch
$\mathcal{L}_{\text{kp}}$	Keypoint detection loss

a) **Temporal Rate Aggregation**: Applying a loss directly to per-timestep spikes  $\mathbf{S}^{(t)} \in \{0, 1\}$  produces unstable gradients. Instead, spikes are aggregated over two temporal windows to obtain smooth rate estimates in  $[0, 1]$ . Let  $T_e = \lfloor \alpha_t T \rfloor$  denote the early window boundary. The early and full window spike rates are:

$$\hat{\mathbf{R}}_e = \frac{1}{T_e} \sum_{t=1}^{T_e} \mathbf{S}_{\text{kp}}^{(t)} \in [0, 1]^{B \times 1 \times H \times W}, \quad (10)$$

$$\hat{\mathbf{R}}_f = \frac{1}{T} \sum_{t=1}^T \mathbf{S}_{\text{kp}}^{(t)} \in [0, 1]^{B \times 1 \times H \times W}. \quad (11)$$

$\hat{\mathbf{R}}_f$  provides the most reliable estimate over the full temporal window, while  $\hat{\mathbf{R}}_e$  ensures early timesteps receive direct gradient supervision rather than only diluted gradients through the full temporal mean.

b) **Two-Point Gaussian Focal Loss**: Standard weighted BCE requires an explicit positive weight estimated from training-set statistics. We instead adopt the focal loss [54] formulation of CornerNet [55], adapted for Gaussian heatmap targets, which handles class imbalance implicitly without requiring explicit positive weights. For a predicted rate map  $\hat{p}$  and Gaussian target  $y \in [0, 1]$ , the per-pixel focal loss is:

$$\ell(y, \hat{p}) = \begin{cases} -(1 - \hat{p})^\alpha \log \hat{p} & \text{if } y = 1, \\ -(1 - y)^\beta \hat{p}^\alpha \log(1 - \hat{p}) & \text{otherwise,} \end{cases} \quad (12)$$

where  $\alpha = 2$  focuses gradient on hard positives, and  $\beta = 4$  down-weights pixels near object centres that are partially positive due to Gaussian spread—preventing them from being penalised as true background. The total is normalised by the number of positive pixels, clamped to a minimum of 1 to handle empty scenes. The two-point focal loss is:

$$\mathcal{L}_{\text{FL}} = \frac{w_e \mathcal{L}_{\text{FL}}(\hat{\mathbf{R}}_e, \mathbf{Y}_{\text{kp}}^*) + w_f \mathcal{L}_{\text{FL}}(\hat{\mathbf{R}}_f, \mathbf{Y}_{\text{kp}}^*)}{w_e + w_f}, \quad (13)$$

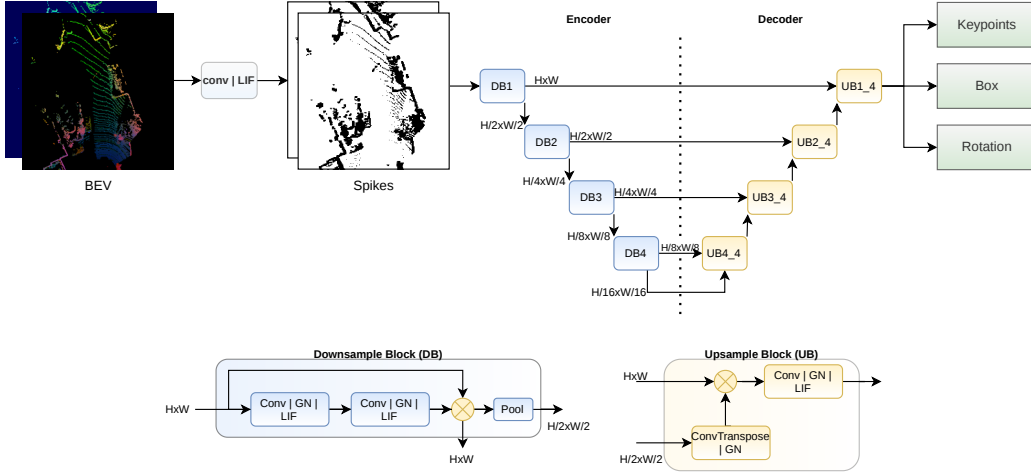


Fig. 1: **Network architecture (top)**: Downsampling Blocks (DB) extract features and reduce spatial resolution while Upsampling Blocks (UB) aggregate multi-scale features and restore spatial resolution. The convolutional layers act as synaptic connections and feature extractors between the Leaky Integrate-and-Fire (LIF) neuron layers.

where  $w_e < w_f$  reflect that the early window is noisier and should contribute less to the primary accuracy signal. Normalisation by  $(w_e + w_f)$  maintains a stable absolute loss scale.

c) *Masked Soft Dice Loss.*: The full-window rate map  $\hat{\mathbf{R}}_f$  is additionally supervised by a masked soft Dice loss [56]. Standard Dice on a sparse BEV map is dominated by background firing in the denominator, rendering it insensitive to whether keypoint peaks are correctly predicted. The Dice computation is therefore restricted to a region of interest  $\mathbf{M}_{\text{roi}}$  obtained by dilating the binary peak mask ( $\mathbf{Y}_{\text{kp}}^* = 1$ ) via max pooling:

$$\mathbf{M}_{\text{roi}} = \text{MaxPool}\left(\mathbb{1}[\mathbf{Y}_{\text{kp}}^* = 1]; \tilde{k}, \lfloor \tilde{k}/2 \rfloor\right), \quad (14)$$

where  $\tilde{k}$  is the smallest odd integer  $\geq k$ , ensuring valid same-size padding. The masked prediction and target are:

$$\tilde{\mathbf{r}}_b = \hat{\mathbf{r}}_b \odot \mathbf{m}_{\text{roi},b}, \quad (15)$$

$$\tilde{\mathbf{y}}_{\text{kp},b}^* = \mathbf{y}_{\text{kp},b}^* \odot \mathbf{m}_{\text{roi},b}, \quad (16)$$

where  $\odot$  denotes element-wise multiplication and lower-case variables denote spatially-flattened vectors of their corresponding maps. The masked Dice loss is:

$$\mathcal{L}_{\text{Dice}} = 1 - \frac{1}{B} \sum_{b=1}^B \frac{2\langle \tilde{\mathbf{r}}_b, \tilde{\mathbf{y}}_{\text{kp},b}^* \rangle + \epsilon}{\|\tilde{\mathbf{r}}_b\|_1 + \|\tilde{\mathbf{y}}_{\text{kp},b}^*\|_1 + \epsilon}, \quad (17)$$

where  $\epsilon > 0$  stabilizes gradients when the ROI is near-empty [57].

d) *Combined Loss with Epoch Gating.*: In early training the network has not yet learned to fire at keypoint locations, so the masked Dice numerator is near zero and its gradient is uninformative. We therefore gate  $\mathcal{L}_{\text{Dice}}$  by training epoch  $e$ :

$$\mathcal{L}_{\text{kp}} = \begin{cases} \mathcal{L}_{\text{FL}} & e < e_{\text{gate}}, \\ \mathcal{L}_{\text{FL}} + \lambda_d \mathcal{L}_{\text{Dice}} & e \geq e_{\text{gate}}, \end{cases} \quad (18)$$

where  $\lambda_d \ll 1$  ensures the masked Dice term provides only structural spatial guidance without destabilising the primary focal signal. In our experiments,  $e_{\text{gate}}$  is set to epoch 40 out of 200 total training epochs, corresponding to the first 20% of training, by which point the focal loss has established a meaningful firing pattern at object centres.

2) *Population-Coded Box Regression Loss*: Estimating continuous physical dimensions—namely length  $l$ , width  $w$ , and height  $h$ —from the sparse binary spike trains produced by a spiking neural network (SNN) presents a fundamental challenge: individual neurons emit stochastic, all-or-nothing pulses that are poorly suited to representing real-valued regression targets in isolation. To address this, we propose a *Population-Coded Box Regression Loss* ( $\mathcal{L}_{\text{box}}$ ) grounded in the principle of population coding [58], wherein a local  $k \times k$  cluster of neurons collectively encodes a single continuous quantity through their aggregate firing activity.

a) *Temporal Rate Integration*: Let  $\mathbf{S}^{(t)} \in \{0, 1\}^{B \times 3 \times H \times W}$  denote the binary spike tensor emitted by the box regression head at timestep  $t$ , where  $B$  is the batch size, 3 corresponds to the three regression targets  $\{l, w, h\}$ , and  $H \times W$  is the spatial resolution of the Bird's-Eye View (BEV) feature map. Over a time window of  $T$  timesteps, we compute the *mean firing rate map*:

$$\hat{\mathbf{R}}_{\text{box}} = \frac{1}{T} \sum_{t=1}^T \mathbf{S}^{(t)} \in [0, 1]^{B \times 3 \times H \times W}, \quad (19)$$

which converts the discrete spike train into a continuous intensity representation amenable to regression supervision.

b) *Spatial Population Integration*: Rather than supervising each spatial neuron independently, we compute the *population consensus* within a local  $k \times k$  neighborhood via average pooling. Let  $b \in \{1, \dots, B\}$  denote the batch index,  $c \in \{l, w, h\}$  the regression channel, and  $(i, j) \in \{1, \dots, H\} \times \{1, \dots, W\}$  the spatial pixel location. The population-pooled prediction is then:

TABLE II: Notation Summary for  $\mathcal{L}_{\text{box}}$ 

Symbol	Description
$T$	Number of timesteps
$k$	Spatial extent of the neuron population cluster
$\mathbf{S}^{(t)}$	Binary spike tensor at timestep $t$
$\hat{\mathbf{R}}_{\text{box}}$	Temporal mean firing rate map
$\hat{\mathbf{R}}_{\text{pop}}$	Population-pooled prediction map
$\mathbf{Y}_{\text{box}}^*$	Ground-truth box dimension map $\{l, w, h\}$
$\mathbf{Y}_{\text{kp}}^*$	Binary keypoint mask
$\mathbf{M}$	Channel-expanded keypoint mask
$\mathcal{L}_{\text{box}}$	Population-coded box regression loss

$$\hat{\mathbf{R}}_{\text{pop}}[b, c, i, j] = \frac{1}{k^2} \sum_{(\delta_i, \delta_j) \in \mathcal{N}_k} \hat{\mathbf{R}}_{\text{box}}[b, c, i + \delta_i, j + \delta_j], \quad (20)$$

where  $\mathcal{N}_k = \{-\lfloor k/2 \rfloor, \dots, \lfloor k/2 \rfloor\}^2$  is the  $k \times k$  local neighborhood centered at pixel  $(i, j)$ . This pooling operation encodes the key insight of population coding: the regression target is satisfied by the *collective mean* of the cluster, permitting individual neurons to exhibit firing variance or intermittent silence while the population as a whole converges to the desired value. Critically, this relaxation stabilizes gradient flow during surrogate-gradient backpropagation [59], where individual spike gradients are noisy approximations of the true gradient.

c) *Masked Regression Objective*: Since box dimensions are only defined at object center locations, the regression loss is restricted to pixels identified as keypoints by the ground-truth keypoint map  $\mathbf{Y}_{\text{kp}}^* \in \{0, 1\}^{B \times H \times W}$ . Let the spatial mask be:

$$\mathbf{M}[b, c, i, j] = \begin{cases} 1 & \text{if } \mathbf{Y}_{\text{kp}}^*[b, i, j] > 0 \\ 0 & \text{otherwise,} \end{cases} \quad (21)$$

expanded across the channel dimension  $c \in \{l, w, h\}$ . The final loss is the  $\ell_1$  norm computed exclusively over the masked keypoint population responses:

$$\mathcal{L}_{\text{box}} = \sum_{b, c, i, j} \mathbf{M}[b, c, i, j] \cdot \left| \hat{\mathbf{R}}_{\text{pop}}[b, c, i, j] - \mathbf{Y}_{\text{box}}^*[b, c, i, j] \right|, \quad (22)$$

where  $\mathbf{Y}_{\text{box}}^* \in \mathbb{R}^{B \times 3 \times H \times W}$  is the ground-truth box dimension map. The  $\ell_1$  norm is chosen over the mean-squared error for its robustness to outliers in physical dimension estimates and its well-behaved gradient magnitude near zero, both of which are critical properties for stable convergence in surrogate-gradient training [60].

If a batch contains no keypoint pixels—corresponding to an empty scene—the loss degenerates gracefully to:

$$\mathcal{L}_{\text{box}} = \mathbf{0}, \quad (23)$$

while preserving the autograd computation graph to prevent silent gradient failures.

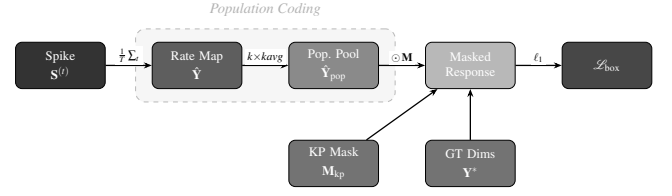


Fig. 2: **Pipeline of the proposed Population-Coded Box Regression Loss**  $\mathcal{L}_{\text{box}}$ : Binary spike trains  $\mathbf{S}^{(t)}$  are temporally integrated into a continuous rate map  $\hat{\mathbf{R}}_{\text{box}}$  (Eq. 19), then spatially pooled over a  $k \times k$  neighborhood to form the population consensus  $\hat{\mathbf{R}}_{\text{pop}}$  (Eq. 20). The  $\ell_1$  regression loss (Eq. 22) is computed solely at object centers defined by the keypoint mask  $\mathbf{Y}_{\text{kp}}^*$ .

3) *Rotation Classification Loss*: Rotation angles are mapped to  $[0, \pi]$  and uniformly discretized into  $C = 31$  bins of  $6^\circ$  each, converting heading estimation into a classification task. The rotation head produces spike trains  $\mathbf{S}_{\text{rot}} \in \{0, 1\}^{T \times B \times C \times H \times W}$ , with one channel per orientation bin across the full BEV spatial map. Since rotation is only defined at object center locations, the loss is restricted to keypoint pixels identified by the ground-truth mask  $\mathbf{Y}_{\text{kp}}^* \in \{0, 1\}^{B \times H \times W}$ .

The temporal mean firing rate across all  $T$  timesteps forms the class logits:

$$\hat{\mathbf{R}}_{\text{rot}} = \frac{1}{T} \sum_{t=1}^T \mathbf{S}_{\text{rot}}^{(t)} \in [0, 1]^{B \times C \times H \times W}. \quad (24)$$

Raw spike rates do not form a valid categorical distribution across bins. A softmax normalization is therefore applied across the channel dimension before computing the cross-entropy, which is handled internally by the cross entropy (CE) loss in the implementation. Let  $\mathbf{y}_{\text{rot}}^* \in \{0, \dots, C-1\}^{B \times H \times W}$  denote the ground-truth bin index map, and let  $\mathbf{w}_c \in \mathbb{R}^C$  be a uniform per-class weight vector that upweights rotation bins relative to background to compensate for the spatial sparsity of object centers. Restricting to keypoint locations via Boolean indexing, the rotation loss is:

$$\mathcal{L}_{\text{rot}} = \text{CE}(\hat{\mathbf{R}}_{\text{rot}}|_{\text{kp}}, \mathbf{y}_{\text{rot}}^*|_{\text{kp}}, \mathbf{w}_c), \quad (25)$$

where  $(\cdot)|_{\text{kp}}$  denotes extraction of predictions and targets at pixels where  $\mathbf{Y}_{\text{kp}}^* = 1$ , and label smoothing  $\varsigma = 0.1$  is applied to reflect the geometric similarity of adjacent orientation bins [61].

## V. EXPERIMENTS AND RESULTS

### A. Dataset, Evaluation Protocol, and Training

We evaluate on the KITTI object detection benchmark [10] using the official train/validation split [63]. Horizontal flipping augmentation is applied selectively to training frames, yielding a total of 6,000 training samples. All models are trained for 200 epochs using Adam [64] with cosine annealing with warm restarts [65] and gradient clipping at  $\|\nabla\|_{\text{max}} = 1.0$  to stabilize surrogate-gradient training [59]. SNNs are implemented in snntorch [11].

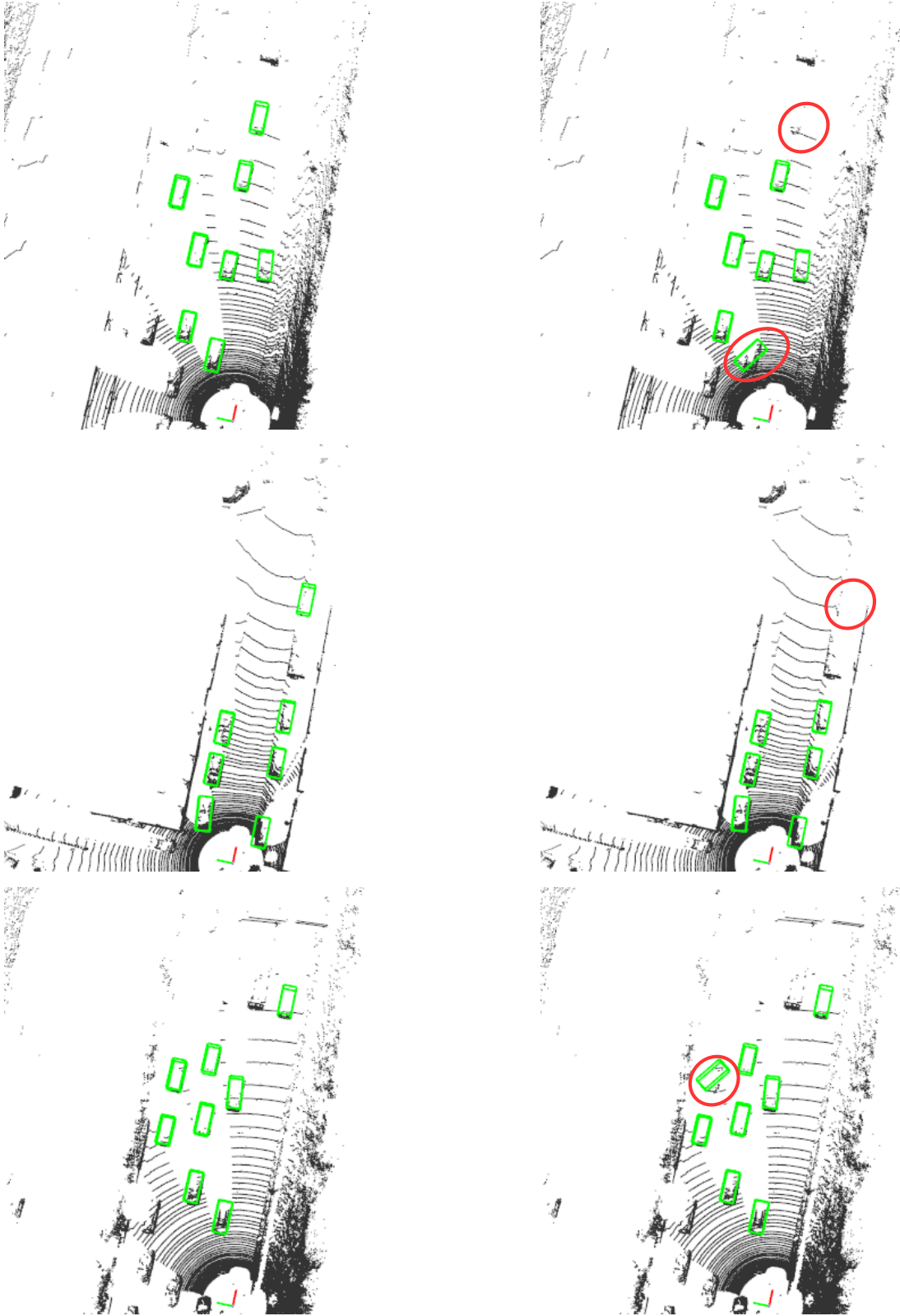


Fig. 3: **Qualitative comparison of 3D object detection on the KITTI validation set across three diverse scenes:** Green boxes denote network predictions. The left column demonstrates the continuous *vmem* readout, while the right column demonstrates the fully binary *spike* readout. Red circles highlight characteristic failure modes induced by purely binary spike inference, including false negatives on distant, sparse objects (top and middle rows) and orientation misalignment (bottom row).

TABLE III: Car Detection Average Precision (AP) on KITTI Validation Set

Type	Model	AP @ IoU=0.5			AP @ IoU=0.7		
		Easy	Mod.	Hard	Easy	Mod.	Hard
CNN	PointPillars [18]	90.78	90.18	89.46	88.32	86.10	79.83
	PointRCNN [15]	90.20	89.63	89.39	92.13	87.39	82.72
	Pixor [20]	89.62	83.45	80.11	86.79	80.75	76.60
	BEVDetNet [21]	87.82	87.78	87.25	82.46	77.90	77.45
SNN	DeepSCNN [44]	—	—	—	71.76	67.43	65.63
	SpikeCloudNet [62]	—	—	—	89.80	84.10	82.70
	SpikiLi [32]	86.37	78.65	78.76	82.71	75.49	68.68
	<b>vmem (ours)</b>	<b>92.05</b>	<b>87.04</b>	<b>86.51</b>	<b>90.11</b>	<b>85.50</b>	<b>82.80</b>
	<b>spike (ours)</b>	88.51	85.72	83.14	85.18	80.20	79.14

TABLE IV: Impact of Input Spike Coding on Average Precision

Encoding	AP @ IoU=0.5		
	Easy	Mod.	Hard
Poisson / rate	87.14	85.83	82.21
Temporal z-axis	78.05	75.44	70.98
Latency	34.62	21.30	10.87
Self-coding	<b>92.05</b>	<b>87.04</b>	<b>86.51</b>

We report AP for the *Car* class at two IoU thresholds across *Easy*, *Moderate*, and *Hard* difficulty levels.  $\text{IoU} = 0.5$  is the operationally relevant threshold for ADAS applications—including collision avoidance, emergency braking, and path planning—where coarse but reliable localization is sufficient for safe decision-making [66].  $\text{IoU} = 0.7$  demands tighter localization and is included for direct comparison with prior work.

### B. Temporal Encoding Strategy

A key design choice in SNN-based perception is how continuous sensor data is converted into spike trains. We evaluate four established strategies [67] in Table IV: Poisson/rate coding, temporal z-axis encoding, latency coding, and self-coding [26]. In self-coding, the same BEV frame is presented identically over  $T = 13$  timesteps, allowing LIF neurons to integrate membrane potential across repeated presentations and converge to a stable internal representation. While this involves frame repetition in offline evaluation, in a deployed system receiving a continuous LiDAR stream each timestep naturally corresponds to a distinct sensor frame, providing a genuine temporal axis without duplication. The static-input results therefore represent a conservative lower bound on real-world performance.

As shown in Table IV, self-coding achieves the highest performance at 92.05/87.04/86.51 AP at  $\text{IoU} = 0.5$ . Poisson/rate coding is the closest alternative at 87.14/85.83/82.21, trailing by approximately 1–4 AP points—a modest but consistent gap attributable to stochastic firing variance introduced by Poisson sampling, which adds noise to the spatial feature representation. Temporal z-axis encoding trails further at 78.05/75.44/70.98, reflecting the loss of within-cell height distribution inherent in collapsing the vertical LiDAR axis into a temporal sequence.

Latency coding collapses to near-chance performance (34.62/21.30/10.87). This is not a tuning failure but a structural incompatibility: latency coding permits at most one spike per neuron over the entire temporal window, inducing extreme activation sparsity from the first layer onward. On dense BEV inputs where most spatial cells carry valid non-zero features, this one-spike constraint destroys the spatial density the architecture depends on and renders surrogate gradient training ineffective, as near-zero gradients propagate through the large fraction of neurons that never reach threshold. Self-coding avoids this pathology by allowing unrestricted firing across timesteps, enabling reliable gradient flow throughout the full spatial extent of the encoder-decoder.

### C. Membrane Potential and Spike Inference Variants

We evaluate two inference variants that together bound the accuracy–deployability trade-off of the proposed architecture. Both variants share identical weights; they differ only in how the output heads produce predictions.

1) **Membrane Potential Variant (vmem)**: The vmem variant reads the final membrane potential  $V_{\text{mem}}$  of the last LIF layer, a continuous quantity accumulating evidence over all  $T$  timesteps. All intermediate layers remain fully spiking, preserving the MAC-to-AC reduction throughout the feature extractor [68]. vmem is compatible with neuromorphic platforms that expose internal membrane state, such as Intel Loihi 2 [3] and IBM TrueNorth [4] in monitoring mode.

vmem (ours) achieves 92.05/87.04/86.51 AP at  $\text{IoU} = 0.5$  and 90.11/85.50/82.80 at  $\text{IoU} = 0.7$  (Easy/Moderate/Hard, Table III), establishing a new state-of-the-art among SNN-based detectors across all difficulty tiers at  $\text{IoU} = 0.7$  and exceeding all CNN baselines on the Easy metric at  $\text{IoU} = 0.5$ . This demonstrates that a spiking backbone with a continuous readout can match and in some cases surpass full-precision CNN counterparts.

2) **Fully Spiking Variant (spike)**: The spike variant replaces the  $V_{\text{mem}}$  readout with predictions derived from the temporal mean firing rate over  $T$  timesteps. Every layer operates exclusively on binary spike trains  $\mathbf{S} \in \{0, 1\}^{T \times H \times W}$ , making spike directly deployable on any event-driven neuromorphic processor without modification, including platforms that do not expose membrane state such as SpiNNaker [5] and BrainScaleS [69].

spike (ours) achieves 88.51/85.72/83.14 AP at  $\text{IoU} = 0.5$  and 85.18/80.20/79.14 at  $\text{IoU} = 0.7$  (Table III), outperforming all prior SNN baselines at  $\text{IoU} = 0.5$ . The 1–3 AP gap relative to vmem quantifies the representational cost of the binary output transition, and is visually evident in Fig. 3. Together, the two variants bound the operating range of the proposed architecture: vmem delivers peak accuracy with minimal hardware assumptions, while spike prioritises full binary compatibility at a modest and well-characterised accuracy cost, without any continuous intermediate activations.

### D. Detection Performance

Table III compares our model against CNN-based and SNN-based detectors. CNN results are included for context. Our

TABLE V: **Block-wise synaptic operation energy comparison:** SNN vs. equivalent CNN. Energy estimated using 45 nm technology constants ( $E_{AC} = 0.9$  pJ,  $E_{MAC} = 4.6$  pJ) at  $T = 13$  timesteps and input resolution  $320 \times 320$ . FR = mean firing rate; Sp. = sparsity ( $1 - \text{FR}$ ); CNN/SNN = energy ratio (higher is better for SNN).

Stage	Block	Input (C×H×W)	MACs	FR	Sp.	Energy ( $\mu\text{J}$ )		Energy Share (%)		CNN/SNN	
						SNN	CNN	SNN	CNN		
Input	Stem	$11 \times 320 \times 320$	162,201,600	0.0183	0.9817	34.7140	746.1274	0.04	0.24	21.49	
	Encoder	DB1	$16 \times 320 \times 320$	2,785,280,000	0.0744	0.9256	2425.4326	12812.2880	2.55	4.04	5.28
		DB2	$48 \times 160 \times 160$	3,632,332,800	0.0873	0.9127	3710.9472	16708.7309	3.90	5.27	4.50
		DB3	$112 \times 80 \times 80$	4,066,918,400	0.0682	0.9318	3244.3032	18707.8246	3.41	5.90	5.77
		DB4	$240 \times 40 \times 40$	4,286,976,000	0.0907	0.9093	4550.8497	19720.0896	4.78	6.22	4.33
	<i>Subtotal</i>	—	14,771,507,200	0.0806	0.9194	13931.5329	67948.9331	14.64	21.44	4.88	
Decoder	UB4_4	$496 \times 20 \times 20$	8,659,763,200	0.1231	0.8769	12475.0975	39834.9107	13.11	12.57	3.19	
	UB3_4	$496 \times 40 \times 40$	16,472,473,600	0.1414	0.8586	27253.3480	75773.3786	28.64	23.91	2.78	
	UB2_3	$240 \times 80 \times 80$	14,981,529,600	0.0933	0.9067	16346.0321	68915.0362	17.18	21.74	4.22	
	UB1_2	$112 \times 160 \times 160$	12,215,910,400	0.1295	0.8705	18507.2248	56193.1878	19.45	17.73	3.04	
		<i>Subtotal</i>	—	52,329,676,800	0.1218	0.8782	74581.7025	240716.5133	78.37	75.95	3.23
Output	Keypoint	$48 \times 320 \times 320$	532,070,400	0.3485	0.6515	2169.7737	2447.5238	2.28	0.77	1.13	
	Box	$48 \times 320 \times 320$	534,528,000	0.3465	0.6535	2166.8515	2458.8288	2.28	0.78	1.13	
	Rotation	$48 \times 320 \times 320$	568,934,400	0.3434	0.6566	2285.8559	2617.0982	2.40	0.83	1.14	
		<i>Subtotal</i>	—	1,635,532,800	0.3461	0.6539	6622.4811	7523.4509	6.96	2.37	1.14
	<b>Total</b>	—	68,898,918,400	0.1181	0.8819	95170.4304	316935.0246	100.00	100.00	<b>3.33</b>	

primary claim is not to surpass full-precision CNNs in raw accuracy, but to demonstrate that SNNs can approach their performance while delivering substantial energy efficiency gains, as quantified in Section V-E.

Among SNN methods, vmem (ours) achieves highly competitive performance across all reported methods, surpassing SpikiLi [70] by +7.68 Moderate and +7.73 Hard AP at  $IoU = 0.5$ . At  $IoU = 0.7$ , the vmem variant establishes a new state-of-the-art among SNN methods on all three difficulty tiers, achieving 90.11 Easy, 85.50 Moderate, and 82.80 Hard AP, surpassing SpikeCloudNet [43]. The fully binary spike variant also demonstrates strong performance, outperforming DeepSCNN [24] and SpikiLi [70] across all metrics at  $IoU = 0.7$  despite relying exclusively on binary outputs rather than continuous readouts.

The performance gap between vmem and spike—approximately 3–4 AP points at  $IoU = 0.5$  and 4–5 AP points at  $IoU = 0.7$  directly quantifies the representational cost of the final continuous-to-binary transition. This gap is visually evident in Fig. 3, where the fully binary *spike* variant exhibits characteristic failure modes on distant, sparse objects and occasional orientation misalignments compared to the tighter localization of the continuous *vmem* readout. Importantly, this gap is substantially narrower than the typical SNN-to-CNN accuracy gap reported in the prior literature [70], which we attribute to the proposed spike-domain loss functions: the two-point temporal BCE and Dice loss for keypoint detection, and the population-coded regression loss for bounding box dimensions. These losses supervise the network directly in the binary spike domain without requiring continuous intermediate activations, enabling gradient information to flow effectively across the full temporal depth of the spiking encoder-decoder.

Relative to CNNs, vmem (ours) achieves 92.05 Easy AP at  $IoU = 0.5$ , exceeding all four CNN baselines on this metric. At  $IoU = 0.7$ , vmem exceeds BEVDetNet [21] by +7.70 Moderate AP and approaches PointPillars [18] (86.10) and PointRCNN [15] (87.39) on the Moderate tier, despite operating with binary spike activations in all intermediate layers. This result suggests that the primary accuracy bottleneck in our architecture is the binary output readout rather than the spiking feature extractor, motivating future work on improved spike-to-prediction decoding at the output stage.

### E. Energy Efficiency Analysis

1) **MAC Count Derivation:** For a convolutional layer with  $C_{in}$  input channels,  $C_{out}$  output channels, kernel size  $K \times K$ , and output spatial resolution  $H_{out} \times W_{out}$ , the MAC count is:

$$N_{MAC} = C_{in} \times K^2 \times C_{out} \times H_{out} \times W_{out}. \quad (26)$$

Bias additions are excluded following standard convention, as their contribution is negligible for all  $C_{in} \geq 2$ ,  $K \geq 3$ .

Each downsampling block (DB) in the encoder comprises three convolutional layers: a  $5 \times 5$  feature extraction convolution (c1), a  $3 \times 3$  refinement convolution (c2), and a strided  $3 \times 3$  pooling convolution (pool) that halves the spatial resolution. The skip connection concatenates the c2 output with the block input along the channel dimension before the pooling convolution. We verify the MAC count for DB1 with input  $16 \times 320 \times 320$  (the stem output):

$$a) \text{ c1: } Conv2d(16 \rightarrow 32, 5 \times 5) \text{ at } 320 \times 320:$$

$$N_{MAC}^{c1} = 16 \times 5^2 \times 32 \times 320 \times 320 = 1,310,720,000. \quad (27)$$

b)  $c_2$ :  $\text{Conv2d}(32 \rightarrow 32, 3 \times 3)$  at  $320 \times 320$ :

$$N_{\text{MAC}}^{c_2} = 32 \times 3^2 \times 32 \times 320 \times 320 = 943,718,400. \quad (28)$$

The output of  $c_2$  is concatenated with the 16-channel block input, yielding a 48-channel feature map ( $32+16 = 48$ ) passed to the pooling convolution.

c)  $\text{pool}$ :  $\text{Conv2d}(48 \rightarrow 48, 3 \times 3, \text{stride} = 2)$  at  $160 \times 160$ :

$$N_{\text{MAC}}^{\text{pool}} = 48 \times 3^2 \times 48 \times 160 \times 160 = 530,841,600. \quad (29)$$

Summing all three layers gives the aggregate MAC count for DB1:

$$\begin{aligned} N_{\text{MAC}}^{\text{DB1}} &= N_{\text{MAC}}^{c_1} + N_{\text{MAC}}^{c_2} + N_{\text{MAC}}^{\text{pool}} \\ &= 1,310,720,000 + 943,718,400 + 530,841,600 \\ &= 2,785,280,000, \end{aligned} \quad (30)$$

exactly matching the value reported in Table V. The same procedure applied to DB2–DB4, the decoder blocks, and the output heads recovers all remaining entries in the table, confirming the internal consistency of the MAC estimates. The channel widths expand progressively at each encoder stage: DB1 outputs 48 channels, DB2 outputs 112, DB3 outputs 240, and DB4 outputs 496, reflecting the progressive feature expansion of the U-Net encoder.

2) **From Multiply-Accumulate to Accumulate-Only Operations**: The fundamental energy advantage of spiking networks over conventional CNNs originates at the level of the individual synaptic operation. In a CNN, every connection between two feature maps requires a *multiply-accumulate* (MAC) operation: the presynaptic activation (a continuous floating-point value) is multiplied by the synaptic weight before being summed into the postsynaptic neuron. In an SNN, presynaptic activations are binary spikes  $s \in \{0, 1\}$ . A spike value of zero contributes nothing to the postsynaptic neuron and requires no computation. A spike value of one simply *accumulates* the weight directly, with no multiplication required. Every MAC is therefore replaced by a cheaper *accumulate-only* (AC) operation.

Using 45 nm technology constants [6]—the established reference node in neuromorphic energy analysis [4], [68]—this distinction carries a concrete energy cost:  $E_{\text{MAC}} = 4.6$  pJ versus  $E_{\text{AC}} = 0.9$  pJ—a **5.1× reduction per active synaptic event**. This saving is not an approximation or a systems-level engineering trick; it is a direct consequence of eliminating the multiplier circuit from the datapath, and applies identically on digital neuromorphic hardware [4], mixed-signal platforms [69], and estimated CMOS implementations [68].

3) **Energy Model**: For a layer with  $N_{\text{MAC}}$  synaptic connections, CNN inference energy is:

$$E_{\text{CNN}} = N_{\text{MAC}} \cdot E_{\text{MAC}}. \quad (31)$$

In the SNN, synaptic events occur only when a presynaptic neuron fires. Over  $T$  timesteps with mean firing rate  $\bar{r}$ , the expected number of active synaptic events is  $N_{\text{MAC}} \cdot \bar{r} \cdot T$ , each costing  $E_{\text{AC}}$ :

$$E_{\text{SNN}} = N_{\text{MAC}} \cdot \bar{r} \cdot T \cdot E_{\text{AC}}. \quad (32)$$

The energy ratio between the two is:

$$\frac{E_{\text{CNN}}}{E_{\text{SNN}}} = \frac{E_{\text{MAC}}}{\bar{r} \cdot T \cdot E_{\text{AC}}} = \frac{4.6}{\bar{r} \times 13 \times 0.9}. \quad (33)$$

Equation 33 reveals two independent levers for energy reduction: the fixed  $5.1 \times$  MAC-to-AC gain, and a further  $1/(\bar{r} \cdot T)$  gain from spike sparsity. These multiply together, so even moderate sparsity yields substantial savings. At the network-wide mean firing rate of  $\bar{r} = 0.1181$ , Eq. 33 predicts a ratio of  $4.6 / (0.1181 \times 13 \times 0.9) = 3.33 \times$ , exactly matching the measured total in Table V.

As a concrete block-level example, consider encoder block DB4 with  $N_{\text{MAC}} = 4,286,976,000$  and  $\bar{r} = 0.0907$ :

$$E_{\text{CNN}}^{\text{DB4}} = 4,286,976,000 \times 4.6 \text{ pJ} = 19,720 \mu\text{J}, \quad (34)$$

$$E_{\text{SNN}}^{\text{DB4}} = 4,286,976,000 \times 0.0907 \times 13 \times 0.9 \text{ pJ} = 4,551 \mu\text{J}, \quad (35)$$

a  $4.33 \times$  reduction, driven by the MAC-to-AC substitution combined with DB4’s low firing rate of 9.07%.

4) **Network-Wide Results**: Table V reports block-wise energy for all stages at input resolution  $320 \times 320$  with  $T = 13$  timesteps. Total SNN inference energy is **95,170  $\mu\text{J}$**  versus **316,935  $\mu\text{J}$**  for the equivalent CNN—an overall **3.33× reduction**, meaning the SNN consumes less than one third of the energy at identical task complexity and resolution. It is important to note that this estimate is conservative: it is derived from loop-based simulation in which the input is presented  $T = 13$  times, counting energy for each pass. On dedicated neuromorphic hardware, the  $T$  timesteps unfold naturally along the temporal dimension of the input stream, eliminating the loop overhead entirely. In that setting the effective energy advantage scales to  $3.33 \times 13 \approx 43 \times$  relative to a single-pass CNN.

The network exhibits a mean firing sparsity of **88.19%** ( $\bar{r} = 0.1181$ ): on average, fewer than 1 in 8 neurons fires at any given timestep.

Fig. 4 illustrates this sparsity qualitatively for the keypoint detection head. The binary spike maps at individual timesteps are highly sparse, with activity concentrating progressively around object-center locations as evidence accumulates across the simulation window. Notably, even with only  $T = 5$  timesteps shown, the temporal mean firing rate map (*avg*) already exhibits clearly elevated activity at vehicle locations in the bird’s eye view input (*BEV*)—demonstrating that the network converges to a meaningful spatial representation rapidly, well within the full  $T = 13$  timestep budget.

As shown in Fig. 5, this sparsity is not a fixed property of the architecture but an *emergent* result of training: the mean firing rate decreases monotonically from 0.356 at epoch 0 to 0.118 at epoch 189, indicating that the network progressively learns sparser spike representations as it converges. Since inactive neurons contribute exactly zero synaptic operations, this sparsity acts as a second independent multiplier on the energy savings already provided by the MAC  $\rightarrow$  AC substitution. Together, these two mechanisms account for the full  $3.33 \times$  gain.

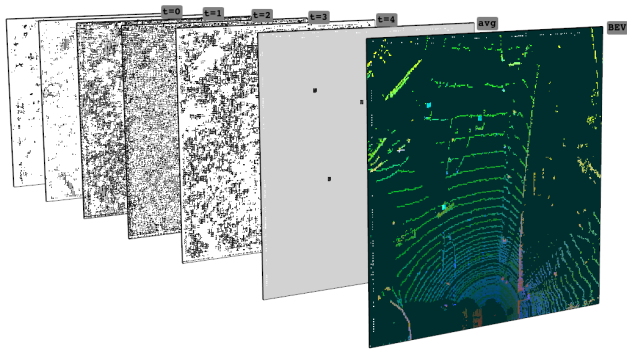


Fig. 4: **Spike activity over time for 5 time steps and spike rate for the keypoint detection head:** Each plane shows the binary spike pattern at a single timestep ( $t = 0$  through  $t = 4$ ), followed by the temporal mean firing rate (*avg*) and the bird’s-eye-view LiDAR input (*BEV*). Cyan spots on the BEV highlight spatial regions with elevated average spike activity.

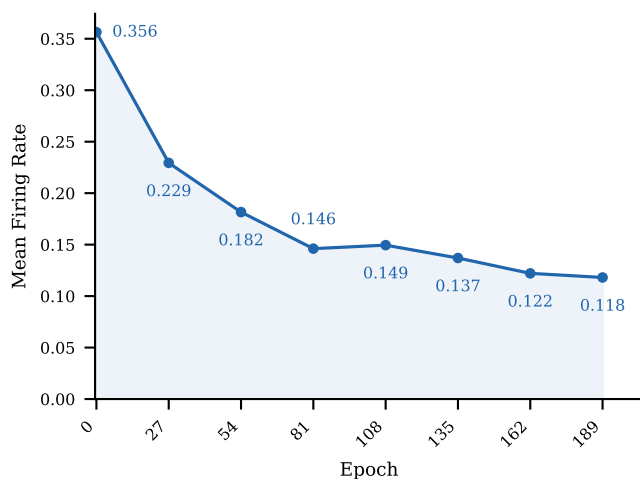


Fig. 5: **Mean firing rate of the proposed SNN across training epochs:** The network learns progressively sparser spike representations.

The decoder dominates SNN energy at 78.37%, driven by the large MAC counts of the transposed convolution upsampling blocks operating at progressively higher spatial resolutions. UB3\_4 alone accounts for 28.64% of total SNN energy, yet still achieves 2.78 $\times$  over its CNN equivalent. The encoder attains 4.88 $\times$  overall, with DB3 reaching 5.77 $\times$  as the most efficient encoder block. The three output heads together account for only 6.96% of total SNN energy—confirming that the multi-task prediction overhead (keypoint, bounding box, and rotation heads) is negligible relative to the backbone, an important property for scaling to additional detection tasks.

#### F. Limitations

Consistent with [21], heading direction is not predicted, following the BEV benchmarking convention that exploits orientation symmetry. The self-coding strategy does not exploit

temporal variation between consecutive LiDAR scans. In a deployed streaming system this limitation is naturally resolved, but multi-frame training to leverage motion cues remains an avenue for future work. On-chip profiling of the spike variant on physical neuromorphic hardware would further validate the energy estimates reported here.

## VI. CONCLUSION

We presented an end-to-end spiking encoder-decoder network for LiDAR bird’s eye view 3D object detection trained with surrogate gradients, offering two inference variants: a membrane potential variant (*vmem*) for maximum accuracy and a fully binary spiking variant (*spike*) for direct neuromorphic deployment. The *vmem* variant achieves 92.05/87.04/86.51 AP at  $IoU = 0.5$  and 90.11/85.50/82.80 at  $IoU = 0.7$ , establishing a new state-of-the-art among SNN-based detectors and approaching full-precision CNN baselines. The *spike* variant achieves 88.51/85.72/83.14 AP at  $IoU = 0.5$  using exclusively binary activations, outperforming all prior SNN-based BEV detectors at this threshold.

Two novel spike-domain loss functions were central to these results: a two-point temporal BCE and masked Dice loss for keypoint detection operating directly on heatmap targets, and a population-coded regression loss for bounding box estimation that eliminates the need to discretise continuous targets. Together, these losses enable gradient information to flow effectively across the full temporal depth of the spiking encoder-decoder without requiring continuous intermediate activations.

A block-wise energy analysis at  $320 \times 320$  input resolution confirms a 3.33 $\times$  reduction in synaptic operation energy over an equivalent CNN, driven by the MAC  $\rightarrow$  AC operation substitution and 88.19% network-wide firing sparsity, both emerging naturally from training without explicit regularisation. This estimate is conservative: on dedicated neuromorphic hardware where  $T$  timesteps unfold naturally along the input stream rather than through explicit simulation loops, the effective energy advantage scales to approximately 43 $\times$ .

The primary avenue for future work is realising true event-driven inference by developing sparse convolution primitives that restrict computation to the spatial neighbourhoods of active spike events, converting the theoretical MAC  $\rightarrow$  AC saving into a measured reduction in runtime and on-chip energy. Additional directions include multi-frame training to exploit temporal variation between consecutive LiDAR scans, on-chip profiling to validate the energy estimates against measured silicon power, and a study of the accuracy–energy trade-off as a function of the simulation timestep budget  $T$ .

## REFERENCES

- [1] L. Joseph and A. K. Mondal, *Autonomous driving and advanced driver-assistance systems (ADAS): applications, development, legal issues, and testing*. CRC Press, 2021.
- [2] V. R. Kumar, S. Milz, C. Witt, M. Simon, K. Amende, J. Petzold, S. Yogamani, and T. Pech, “Near-field depth estimation using monocular fisheye camera: A semi-supervised learning approach using sparse lidar data,” in *CVPR Workshop*, vol. 7, 2018, p. 2.

- [3] G. Orchard, E. P. Frady, D. B. Rubin, S. Sanborn, S. B. Shrestha, F. T. Sommer, and M. Davies, "Efficient neuromorphic signal processing with Loihi 2," in *IEEE Workshop on Signal Processing Systems (SiPS)*, 2021, pp. 254–259.
- [4] P. A. Merolla, J. V. Arthur, R. Alvarez-Icaza, A. S. Cassidy, J. Sawada, F. Akopyan, B. L. Jackson, N. Imam, C. Guo, Y. Nakamura *et al.*, "A million spiking-neuron integrated circuit with a scalable communication network and interface," *Science*, vol. 345, no. 6197, pp. 668–673, 2014.
- [5] S. B. Furber, F. Galluppi, S. Temple, and L. A. Plana, "The SpiNNaker project," vol. 102, no. 5, 2014, pp. 652–665.
- [6] M. Horowitz, "1.1 computing's energy problem (and what we can do about it)," in *IEEE International Solid-State Circuits Conference (ISSCC)*, 2014, pp. 10–14.
- [7] Y. Li and J. Ibanez-Guzman, "LiDAR for autonomous driving: The principles, challenges, and trends for automotive LiDAR and perception systems," *IEEE Signal Processing Magazine*, vol. 37, no. 4, pp. 50–61, 2020.
- [8] G. Gallego, T. Delbrück, G. Orchard, C. Bartolozzi, B. Tabá, A. Censi, S. Leutenegger, A. J. Davison, J. Conradt, K. Daniilidis *et al.*, "Event-based vision: A survey," *IEEE transactions on pattern analysis and machine intelligence*, vol. 44, no. 1, pp. 154–180, 2020.
- [9] J. Schramm, N. Vödisch, K. Petek, B. R. Kiran, S. Yogamani, W. Burgard, and A. Valada, "BevcAR: Camera-radar fusion for bev map and object segmentation," in *2024 IEEE/RSJ International Conference on Intelligent Robots and Systems (IROS)*. IEEE, 2024, pp. 1435–1442.
- [10] A. Geiger, P. Lenz, C. Still, and R. Urtasun, "Vision meets robotics: The kitti dataset," *The international journal of robotics research*, vol. 32, no. 11, pp. 1231–1237, 2013.
- [11] J. K. Eshraghian, M. Ward, E. O. Neftci, X. Wang, G. Lenz, G. Dwivedi, M. Bennamoun, D. S. Jeong, and W. D. Lu, "Training spiking neural networks using lessons from deep learning," *Proceedings of the IEEE*, vol. 111, no. 9, pp. 1016–1054, 2023.
- [12] M. Engelcke, D. Rao, D. Z. Wang, C. H. Tong, and I. Posner, "Vote3deep: Fast object detection in 3d point clouds using efficient convolutional neural networks," in *2017 IEEE International Conference on Robotics and Automation (ICRA)*. IEEE, 2017, pp. 1355–1361.
- [13] Y. Zhou and O. Tuzel, "Voxelnet: End-to-end learning for point cloud based 3d object detection," in *Proceedings of the IEEE conference on computer vision and pattern recognition*, 2018, pp. 4490–4499.
- [14] Y. Yan, Y. Mao, and B. Li, "Second: Sparsely embedded convolutional detection," *Sensors*, vol. 18, no. 10, p. 3337, 2018.
- [15] S. Shi, X. Wang, and H. Li, "PointRCNN: 3d object proposal generation and detection from point cloud," in *Proceedings of the IEEE/CVF conference on computer vision and pattern recognition*, 2019, pp. 770–779.
- [16] C. R. Qi, L. Yi, H. Su, and L. J. Guibas, "Pointnet++: Deep hierarchical feature learning on point sets in a metric space," *Advances in neural information processing systems*, vol. 30, 2017.
- [17] S. Shi, C. Guo, L. Jiang, Z. Wang, J. Shi, X. Wang, and H. Li, "Pv-rcnn: Point-voxel feature set abstraction for 3d object detection," in *Proceedings of the IEEE/CVF conference on computer vision and pattern recognition*, 2020, pp. 10 529–10 538.
- [18] A. H. Lang, S. Vora, H. Caesar, L. Zhou, J. Yang, and O. Beijbom, "Pointpillars: Fast encoders for object detection from point clouds," in *Proceedings of the IEEE/CVF conference on computer vision and pattern recognition*, 2019, pp. 12 697–12 705.
- [19] C. R. Qi, H. Su, K. Mo, and L. J. Guibas, "Pointnet: Deep learning on point sets for 3d classification and segmentation," in *Proceedings of the IEEE conference on computer vision and pattern recognition*, 2017, pp. 652–660.
- [20] B. Yang, W. Luo, and R. Urtasun, "PIXOR: Real-time 3D object detection from point clouds," in *Proceedings of the IEEE Conference on Computer Vision and Pattern Recognition (CVPR)*, 2018, pp. 7652–7660.
- [21] S. Mohapatra, S. Yogamani, H. Gotzlig, S. Milz, and P. Mader, "Bevdetnet: Bird's eye view lidar point cloud based real-time 3d object detection for autonomous driving," in *2021 IEEE International Intelligent Transportation Systems Conference (ITSC)*. IEEE, 2021, pp. 2809–2815.
- [22] A. Y. Naich and J. R. Carrión, "Lidar-based intensity-aware outdoor 3d object detection," *Sensors*, vol. 24, no. 9, p. 2942, 2024.
- [23] K. Lis, T. Kryjak, and M. Gorgoń, "Lift: Lightweight, fpga-tailored 3d object detection based on lidar data," in *International Workshop on Design and Architectures for Signal and Image Processing*. Springer, 2025, pp. 28–40.
- [24] Y. Cao, Y. Chen, and D. Khosla, "Spiking deep convolutional neural networks for energy-efficient object recognition," *International Journal of Computer Vision*, vol. 113, no. 1, pp. 54–66, 2015.
- [25] P. U. Diehl, D. Neil, J. Binas, M. Cook, S.-C. Liu, and M. Pfeiffer, "Fast-classifying, high-accuracy spiking deep networks through weight and threshold balancing," in *2015 International joint conference on neural networks (IJCNN)*. IEEE, 2015, pp. 1–8.
- [26] B. Rueckauer, I.-A. Lungu, Y. Hu, M. Pfeiffer, and S.-C. Liu, "Conversion of continuous-valued deep networks to efficient event-driven networks for image classification," *Frontiers in neuroscience*, vol. 11, p. 682, 2017.
- [27] J. Deng, W. Dong, R. Socher, L.-J. Li, K. Li, and L. Fei-Fei, "Imagenet: A large-scale hierarchical image database," in *2009 IEEE conference on computer vision and pattern recognition*. IEEE, 2009, pp. 248–255.
- [28] A. Krizhevsky, G. Hinton *et al.*, "Learning multiple layers of features from tiny images," University of Toronto, Tech. Rep., 2009.
- [29] S. Kim, S. Park, B. Na, and S. Yoon, "Spiking-yolo: spiking neural network for energy-efficient object detection," in *Proceedings of the AAAI conference on artificial intelligence*, vol. 34, no. 07, 2020, pp. 11 270–11 277.
- [30] M. Uricár, D. Hurych, P. Krizek, and S. Yogamani, "Challenges in designing datasets and validation for autonomous driving," in *Proceedings of the International Joint Conference on Computer Vision, Imaging and Computer Graphics Theory and Applications (VISAPP)*, 2019.
- [31] J. Qu, Z. Gao, T. Zhang, Y. Lu, H. Tang, and H. Qiao, "Spiking neural network for ultralow-latency and high-accurate object detection," *IEEE Transactions on Neural Networks and Learning Systems*, vol. 36, no. 3, pp. 4934–4946, 2024.
- [32] S. Mohapatra, T. Mesquida, M. Hodaei, S. Yogamani, H. Gotzlig, and P. Mäder, "Spikili: A spiking simulation of lidar based real-time object detection for autonomous driving," in *2022 IEEE Intelligent Vehicles Symposium (IV)*. IEEE, 2022, pp. 1118–1125.
- [33] Y. Tao and Q. Wu, "Spiking pointcnn: An efficient converted spiking neural network under a flexible framework," *Electronics*, vol. 13, no. 18, p. 3626, 2024.
- [34] Y. Li, R. Bu, M. Sun, W. Wu, X. Di, and B. Chen, "Pointcnn: Convolution on x-transformed points," in *Advances in Neural Information Processing Systems (NeurIPS)*, vol. 31, 2018, pp. 820–830.
- [35] S. Lan, M. Zhang, Q. Wu *et al.*, "Efficient converted spiking neural network for 3d and 2d classification," in *Proceedings of the IEEE/CVF International Conference on Computer Vision (ICCV)*, 2023, pp. 10 356–10 365.
- [36] E. O. Neftci, H. Mostafa, and F. Zenke, "Surrogate gradient learning in spiking neural networks: Bringing the power of gradient-based optimization to spiking neural networks," *IEEE Signal Processing Magazine*, vol. 36, no. 6, pp. 51–63, 2019.
- [37] Y. Wu, L. Deng, G. Li, J. Zhu, and L. Shi, "Spatio-temporal backpropagation for training high-performance spiking neural networks," *Frontiers in neuroscience*, vol. 12, p. 331, 2018.
- [38] Z. Li, M. Yao, X. Qiu *et al.*, "Brain-inspired spiking neural networks for energy-efficient object detection," in *Proceedings of the IEEE/CVF Conference on Computer Vision and Pattern Recognition (CVPR)*, 2025.
- [39] L. Cordone, B. Miramond, and P. Thierion, "Object detection with spiking neural networks on automotive event data," in *International Joint Conference on Neural Networks (IJCNN)*, 2022, pp. 1–8.
- [40] R.-J. Zhu, Z. Wang, L. Gilpin, and J. K. Eshraghian, "Autonomous driving with spiking neural networks," in *Advances in Neural Information Processing Systems (NeurIPS)*, 2024.
- [41] D. Ren, Z. Ma, Y. Chen, W. Peng, X. Liu, Y. Zhang, and Y. Guo, "Spiking PointNet: Spiking neural networks for point clouds," in *Advances in Neural Information Processing Systems (NeurIPS)*, vol. 36, 2023.
- [42] Q. Wu, Q. Zhang, C. Tan, Y. Zhou, and C. Sun, "Point-to-spike residual learning for energy-efficient 3D point cloud classification," in *Proceedings of the AAAI Conference on Artificial Intelligence*, vol. 38, 2024, pp. 6092–6099.
- [43] H. Ren, Z. Zhao, A. Lombardini, G. Tang, and P. Li, "Spiking PointNet: Spiking neural networks for point clouds," in *Advances in Neural Information Processing Systems (NeurIPS)*, 2023.
- [44] S. Lian, J. Luo, Z. Zhao, S. Li, S. Yu, and L. Deng, "Deep SCNN-based real-time object detection for self-driving vehicles using LiDAR temporal data," *IEEE Access*, vol. 8, pp. 76 903–76 912, 2020.
- [45] W. Maass, "Networks of spiking neurons: the third generation of neural network models," *Neural networks*, vol. 10, no. 9, pp. 1659–1671, 1997.
- [46] E. D. Adrian and Y. Zotterman, "The impulses produced by sensory nerve endings," *The Journal of physiology*, vol. 61, no. 4, pp. 465–483, 1926.
- [47] S. Thorpe and J. Gautrais, "Rapid visual processing using spike asynchrony," *Advances in neural information processing systems*, vol. 9, 1996.

- [48] Q. Su, Y. Chou, Y. Hu, J. Li, S. Mei, Z. Zhang, and G. Li, "Deep directly-trained spiking neural networks for object detection," in *Proceedings of the IEEE/CVF International Conference on Computer Vision*, 2023, pp. 6555–6565.
- [49] A. Pouget, P. Dayan, and R. Zemel, "Information processing with population codes," *Nature Reviews Neuroscience*, vol. 1, pp. 125–132, 2000.
- [50] S. Mohapatra, S. Yogamani, V. R. Kumar, S. Milz, H. Gotzig, and P. Mäder, "Lidar-bevmtn: Real-time lidar bird's-eye view multi-task perception network for autonomous driving," *IEEE transactions on intelligent transportation systems*, vol. 26, no. 2, pp. 1547–1561, 2025.
- [51] S. Mohapatra, M. Hodaie, S. Yogamani, S. Milz *et al.*, "LiMoSeg: Real-time Bird's Eye View based LiDAR Motion Segmentation," in *Proceedings of the 17th International Joint Conference on Computer Vision, Imaging and Computer Graphics Theory and Applications (VISIGRAPP 2022)*, 2022.
- [52] A. Barrera, C. Guindel, J. Beltrán, and F. García, "Birdnet+: End-to-end 3d object detection in lidar bird's eye view," in *2020 IEEE 23rd International Conference on Intelligent Transportation Systems (ITSC)*. IEEE, 2020, pp. 1–6.
- [53] O. Ronneberger, P. Fischer, and T. Brox, "U-net: Convolutional networks for biomedical image segmentation," in *International Conference on Medical image computing and computer-assisted intervention*. Springer, 2015, pp. 234–241.
- [54] T.-Y. Lin, P. Goyal, R. Girshick, K. He, and P. Dollár, "Focal loss for dense object detection," in *Proceedings of the IEEE International Conference on Computer Vision (ICCV)*, 2017, pp. 2980–2988.
- [55] H. Law and J. Deng, "Cornernet: Detecting objects as paired keypoints," in *Proceedings of the European Conference on Computer Vision (ECCV)*, 2018, pp. 734–750.
- [56] F. Milletari, N. Navab, and S.-A. Ahmadi, "V-Net: Fully convolutional neural networks for volumetric medical image segmentation," in *International Conference on 3D Vision (3DV)*, 2016, pp. 565–571.
- [57] C. H. Sudre, W. Li, T. Vercauteren, S. Ourselin, and M. J. Cardoso, "Generalised dice overlap as a deep learning loss function for highly unbalanced segmentations," in *Deep Learning in Medical Image Analysis and Multimodal Learning for Clinical Decision Support (DLMIA)*, 2017, pp. 240–248.
- [58] A. Pouget, P. Dayan, and R. Zemel, "Information processing with population codes," *Nature Reviews Neuroscience*, vol. 1, no. 2, pp. 125–132, 2000.
- [59] E. O. Neftci, H. Mostafa, and F. Zenke, "Surrogate gradient learning in spiking neural networks: Bringing the power of gradient-based optimization to spiking neural networks," *IEEE Signal Processing Magazine*, vol. 36, no. 6, pp. 51–63, 2019.
- [60] J. H. Lee, T. Delbruck, and M. Pfeiffer, "Training deep spiking neural networks using backpropagation," in *Frontiers in Neuroscience*, vol. 10, 2016, p. 508.
- [61] C. Szegedy, V. Vanhoucke, S. Ioffe, J. Shlens, and Z. Wojna, "Rethinking the inception architecture for computer vision," in *Proceedings of the IEEE Conference on Computer Vision and Pattern Recognition (CVPR)*, 2016, pp. 2818–2826.
- [62] M. Neumeier, N. Fasfous, B. Li, and A. von Arnim, "Spikeclouds: Streaming spike-based processing of lidar for fast and efficient object detection," *IEEE Robotics and Automation Letters*, 2025.
- [63] X. Chen, K. Kundu, Z. Zhang, H. Ma, S. Fidler, and R. Urtasun, "Monocular 3D object detection for autonomous driving," in *Proceedings of the IEEE Conference on Computer Vision and Pattern Recognition (CVPR)*, 2016, pp. 2147–2156.
- [64] D. P. Kingma and J. Ba, "Adam: A method for stochastic optimization," *arXiv preprint arXiv:1412.6980*, 2014.
- [65] I. Loshchilov and F. Hutter, "SGDR: Stochastic gradient descent with warm restarts," in *International Conference on Learning Representations (ICLR)*, 2017.
- [66] H. Caesar, V. Bankiti, A. H. Lang, S. Vora, V. E. Liong, Q. Xu, A. Krishnan, Y. Pan, G. Baldan, and O. Beijbom, "nuScenes: A multimodal dataset for autonomous driving," in *Proceedings of the IEEE Conference on Computer Vision and Pattern Recognition (CVPR)*, 2020, pp. 11 621–11 631.
- [67] D. Auge, J. Hille, E. Mueller, and A. Knoll, "A survey of encoding techniques for signal processing in spiking neural networks," *Neural Processing Letters*, vol. 53, pp. 4395–4429, 2021.
- [68] K. Roy, A. Jaiswal, and P. Panda, "Towards spike-based machine intelligence with neuromorphic computing," *Nature*, vol. 575, pp. 607–617, 2019.
- [69] J. Schemmel, D. Brüderle, A. Grübl, M. Hock, K. Meier, and S. Millner, "A wafer-scale neuromorphic hardware system for large-scale neural modeling," in *Proceedings of the IEEE International Symposium on Circuits and Systems (ISCAS)*, 2010, pp. 1947–1950.
- [70] X. Li, P. Bhatt, R. Li, W. Zhang, and U. Bhatt, "SpikiLi: A spiking based LiDAR point cloud object detection model for autonomous driving," in *IEEE International Conference on Acoustics, Speech and Signal Processing (ICASSP)*, 2023.